

Article aeroacoustics

On a stabilization of the Ingard-Myers impedance boundary condition and its time domain implementation

International Journal of Aeroacoustics 2024, Vol. 23(3-4) 318–341
© The Author(s) 2024
Article reuse guidelines:
sagepub.com/journals-permissions
DOI: 10.1177/1475472X241230649
journals.sagepub.com/home/jae

Fang Q Hu o and Douglas M Nark o

Abstract

It has been well-known that the Ingard-Myers impedance condition, while simple to apply, is subject to the hydrodynamic Kelvin-Helmholtz-type instability due to its use of a vortex sheet in modeling the flow at the liner boundary. Recently, in the development of a time domain boundary element method for acoustic scattering by treated surfaces, it was found that by neglecting a certain second-order spatial derivative term in the Ingard-Myers formulation, the hydrodynamic instability can be avoided. The present paper aims to provide further analysis of this modified condition, hereby referred to as the Truncated Ingard-Myers Impedance Boundary Condition (TIMIBC). It will be shown, based on the dispersion relations of linear waves, that the instability intrinsic to the Ingard-Myers condition is eliminated in the proposed new formulation. Quantitative assessments on the accuracy of the TIMIBC for scattering of acoustic waves by lined surfaces are carried out, and its effectiveness is demonstrated by a numerical example. It is found that the TIMIBC provides a good approximation to the original Ingard-Myers condition for flows of low to mid subsonic Mach numbers. As such, the proposed TIMIBC can offer a practical solution for overcoming the intrinsic instability associated with the Ingard-Myers condition. Moreover, time domain implementation of the TIMIBC is also discussed and illustrated with a numerical example using a finite difference scheme. In particular, a minimization procedure for finding the poles and coefficients of a broadband multipole expansion for the impedance function is formulated by which, unlike the commonly used vector-fitting method, passivity of the model is ensured.

Keywords

Time domain impedance boundary condition, Ingard-Myers boundary condition, computational aeroacoustics, Kelvin-Helmholtz instability

Date received: 16 August 2023; accepted: 13 January 2024

The Editor-in-Chief, Dr. Raman, handled this paper independently.

Corresponding author:

Fang Q Hu, Department of Mathematics and Statistics, Old Dominion University, 5115 Hampton BLVD, Department of Math & Stat, Norfolk, VA 23529, USA.

Email: fhu@odu.edu

¹Department of Mathematics and Statistics, Old Dominion University, Norfolk, VA, USA

²Structural Acoustics Branch, Research Directorate, NASA Langley Research Center, Hampton, VA, USA

Introduction

In an influential paper published in 1959, Ingard considered the acoustic boundary condition at a planar lined surface in the presence of a uniform mean flow. A generalization for surfaces of a general shape was later given by Myers. This condition has often been referred to as the Ingard-Myers impedance condition. While the Ingard-Myers condition is simple to apply, one drawback is that it is subject to the hydrodynamic Kelvin-Helmholtz-type instability due to its use of a vortex sheet in modeling the flow at the liner boundary. The instability was first recognized by Tester in a study of sound attenuation in lined ducts. It has been analyzed extensively in many recent studies due to the importance of acoustic liners in reducing engine noise (see, e.g., refs. 4–7). The instability is particularly problematic when the impedance condition is implemented in the time domain where acoustic waves of all frequencies are present. There have been many efforts in the literature to modify the Ingard-Myers condition to reduce or eliminate the instability, often by replacing the vortex sheet with a boundary layer of finite thickness (e.g., refs. 8, 9). Currently, the Ingard-Myers impedance boundary condition is still widely used as the limiting case of the boundary layer thickness going to zero.

Time domain implementation of impedance boundary conditions for Computational Aero-acoustics was first studied by Tam and Auriault.⁴ A three-parameter model that forms a well-posed boundary condition for the linearized Euler equations was proposed for both single-frequency and broadband impedance conditions. The existence of Kelvin-Helmholtz-type instability in the Ingard-Myers condition was also shown analytically. Since the work of Tam and Auriault, the three-parameter model has been steadily improved and it is now common to use a multipole expansion for modeling the impedance function. ^{10–13}

Recently, in the development of a time domain boundary element method for acoustic scattering by lined surfaces, it was found that by neglecting a certain second-order spatial derivative term in the Ingard-Myers formulation, the hydrodynamic instability can in fact be avoided. ¹⁴ The present paper aims to provide further analysis of this modified Ingard-Myers condition, hereby referred to as the Truncated Ingard-Myers Impedance Boundary Condition (TIMIBC). A quantitative assessment on the accuracy of the TIMIBC for the scattering of acoustic waves by lined surfaces will be carried out, and its effectiveness will be demonstrated by a numerical example. It will be shown, based on the dispersion relations of intrinsic linear waves, that the instability waves of the Ingard-Myers condition are eliminated in the proposed new formulation. The accuracy of the modified condition is assessed by comparing the theoretical reflection coefficients at a lined surface obtained by the Ingard-Myers condition with that by the TIMIBC for cases of plane and spherical incident waves.

Acoustical properties of a liner are characterized by the impedance value in the frequency domain. In this work, liner impedance as a function of frequency is modeled by a broadband multipole expansion. The multipole expansion that matches the experimentally measured/educed impedance is often computed using the vector-fitting method. The vector-fitting method converts a nonlinear optimization problem to a series of linear least square problems. However, a drawback of the vector-fitting method is that the passivity condition is not ensured and needs to be separately checked or enforced. In this paper, we describe a minimization method for finding the poles and coefficients of the multipole model in which passivity is always satisfied.

The rest of the paper is organized as follows. In the next section, the Ingard-Myers impedance condition is reviewed and the proposed TIMIBC is described. It is followed by a theoretical proof for the stability of the TIMIBC. Then an assessment on the accuracy of the TIMIBC using analytical solutions of acoustic reflection by lined surfaces with flow is conducted. Issues related to the time domain implementation of the TIMIBC are discussed and a numerical example is presented.

The Ingard-Myers impedance condition and the proposed stabilization

In the Ingard-Myers impedance model for a liner with flow, an infinitely thin vortex sheet is introduced between the moving fluid and the lined surface, as shown in Figure 1. It is assumed that acoustic pressure will induce an infinitesimally small fluctuation on the liner surface which, upon linearization, satisfies the impedance condition:

$$\frac{\widehat{p}(\mathbf{r},\omega)}{\widehat{u}_{\mathbf{w}}(\mathbf{r},\omega)} = Z(\omega),\tag{1}$$

where p is the pressure of the acoustic wave and $u_{\rm w}$ is the velocity of the lined surface in the direction n that is normal to the undisturbed surface and pointing out of the domain of the fluid. Here, r = (x, y, z) is the position vector, $Z(\omega)$ denotes the impedance of the lined surface at frequency ω , and a caret has been used to denote variables in the frequency domain.

Let the displacement of the vortex sheet in the normal direction n be denoted as

$$\zeta = \zeta(\mathbf{r}, t). \tag{2}$$

Then, we have

$$u_{\rm w} = \frac{\partial \zeta}{\partial t}.\tag{3}$$

On the other hand, under the assumption of a constant uniform flow U in the direction of x, i.e., U = (U, 0, 0), the linearized acoustic velocity of the fluid in the direction of n normal to the vortex sheet, denoted by u_n , is

$$u_n = \frac{\partial \zeta}{\partial t} + U \frac{\partial \zeta}{\partial x}.$$
 (4)

Here, continuity of displacement is applied based on the inviscid fluid assumption as discussed in ref. 17. Eliminating ζ , we get a relation between u_n and u_w as

$$\frac{\partial u_n}{\partial t} = \frac{\partial u_w}{\partial t} + U \frac{\partial u_w}{\partial x}.$$
 (5)

Using equation (5), and assuming $Z(\omega)$ to be constant along the liner, the impedance condition (equation (1)) can now be expressed in the frequency domain as

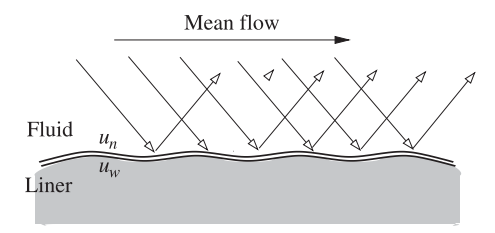


Figure 1. Illustration of Ingard-Myers liner vortex sheet model. u_n and u_w are normal velocities of the fluid and liner surface, respectively.

$$\left(-i\omega + U\frac{\partial}{\partial x}\right)\widehat{p}(\mathbf{r},\omega) = -i\omega Z(\omega)\widehat{u}_n(\mathbf{r},\omega),\tag{6}$$

where a time dependency of $e^{-i\omega t}$ is assumed. Now by the Euler equations for inviscid fluids, we have the following relation between u_n and the normal acoustic pressure derivative $\partial p/\partial n$:

$$\frac{\partial u_n}{\partial t} + U \frac{\partial u_n}{\partial x} + \frac{1}{\rho_0} \frac{\partial p}{\partial n} = 0, \tag{7}$$

where ρ_0 is the mean density of the fluid. Then, the Ingard-Myers impedance condition (6) can also be expressed as

$$\rho_0 \left(-i\omega + U \frac{\partial}{\partial x} \right)^2 \widehat{p}(\mathbf{r}, \omega) = i\omega Z(\omega) \frac{\partial \widehat{p}}{\partial n}(\mathbf{r}, \omega). \tag{8}$$

It has been well-known that the Ingard-Myers condition, for all its equivalent forms (equations (1), (6) and (8)), can cause instability waves in numerical simulations, especially in time domain calculations where acoustic waves of all frequencies are included in the computation. In an effort to mitigate or remove this instability, we note that, upon expanding the second-order convective derivative operator in equation (8), we have

$$\rho_0 \left((-i\omega)^2 \widehat{p} + 2(-i\omega) U \frac{\partial \widehat{p}}{\partial x} + U^2 \frac{\partial^2 \widehat{p}}{\partial x^2} \right) = i\omega Z(\omega) \frac{\partial \widehat{p}}{\partial n}. \tag{9}$$

In a recent study of time domain boundary element methods with impedance boundary conditions, it was found that when the term $U^2 \frac{\partial^2 p}{\partial x^2}$ in equation (9) was dropped from the formulation, the instability can actually be avoided. Discarding the $U^2 \frac{\partial^2 p}{\partial x^2}$ term in equation (9) and simplifying, we get the following proposed *Truncated Ingard-Myers Impedance Boundary Condition* (TIMIBC):

$$-\rho_0 \left((-i\omega)\widehat{p} + 2U \frac{\partial \widehat{p}}{\partial x} \right) = Z(\omega) \frac{\partial \widehat{p}}{\partial n}. \tag{10}$$

When written in pressure p and normal acoustic velocity u_n at the boundary, the TIMIBC (equation (10)) can be expressed as follows:

$$(-i\omega)\widehat{p} + 2U\frac{\partial\widehat{p}}{\partial x} = Z(\omega)\left((-i\omega)\widehat{u}_n + U\frac{\partial\widehat{u}_n}{\partial x}\right),\tag{11}$$

where use has been made of the relation given in equation (7).

The stability and accuracy of this truncated Ingard-Myers condition will be the main subject of study for the present paper.

Dispersion relations and linear stability analysis

In this section, we show that the TIMIBC given in equation (10) removes the instability wave of the original Ingard-Myers formulation. Suppose we look for acoustic solutions of the following form in the semi-infinite domain $z \ge 0$ above a lined surface located at z = 0:

$$\widehat{p}(\mathbf{r},\omega) = Ae^{ik_x x + ik_y y + i\gamma z - i\omega t},\tag{12}$$

where

$$\gamma = \sqrt{\left(\omega/c - Mk_x\right)^2 - \left(k_x^2 + k_y^2\right)},\tag{13}$$

M = U/c is the mean flow Mach number, and c is the speed of sound. In this paper, only subsonic flows are considered, i.e., we assume M < 1. The branch-cut in the complex ω plane for the square-root function in equation (13) is such that

$$\operatorname{Im}\left\{\sqrt{(\omega/c - Mk_{x})^{2} - \left(k_{x}^{2} + k_{y}^{2}\right)}\right\} \ge 0. \tag{14}$$

Throughout this paper, Re $\{\cdot\}$ and Im $\{\cdot\}$ denote respectively the real and imaginary parts of the expression inside the bracket. Equation (12) represents a solution to the convective wave equation that satisfies the outgoing condition at $z \to +\infty$.

Applying the Ingard-Myers impedance boundary condition (equation (8)) at z = 0 to the solution given in equation (12) leads readily to the following dispersion relation equation, denoted as $D_{IM}(\omega, k_x, k_y)$, for linear waves supported by the Ingard-Myers condition:

$$D_{IM}(\omega, k_x, k_y) \equiv (\omega/c)\gamma Z + \rho_0 c(\omega/c - Mk_x)^2 = 0.$$
(15)

As noted earlier, numerous studies have shown that the dispersion relation (equation (15)) can support instability waves (e.g., refs. 3–7). That is, given real values of k_x and k_y , equation (15) entails roots for ω with a positive imaginary part, i.e., $\text{Im}\{\omega\} > 0$. Figure 2(a) shows an example of an unstable root in the dispersion relation equation (equation (15)). Plotted are the level curves of $\text{Re}\{D_{IM}(\omega,k_x,k_y)\}=0$, in solid lines, and $\text{Im}\{D_{IM}(\omega,k_x,k_y)\}=0$, in dashed lines, on the complex ω plane where the wave numbers are fixed at $k_x=1$ and $k_y=0$. For this example, the value for the nondimensional impedance is $Z/\rho_0c=0.5+0.1i$ and the Mach number M=0.5. Any intersection point of these two sets of level curves, therefore, represents a root for the dispersion equation $D_{IM}(\omega,k_x,k_y)=0$. In this particular case, Figure 2(a) clearly shows the existence of an unstable root in the upper half ω plane, as denoted by a circle in the figure. This demonstrates, indeed, the Ingard-Myers

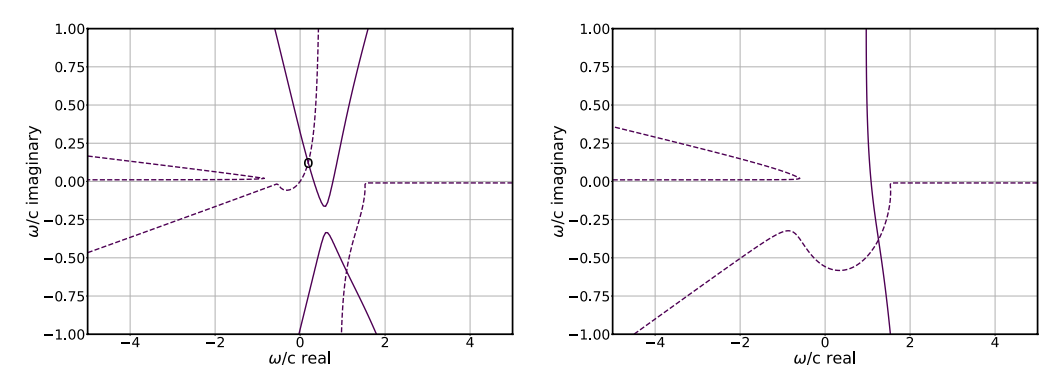


Figure 2. Contours of (a) $D_{IM}(\omega, k_x, k_y) = 0$ and (b) $D_{TIM}(\omega, k_x, k_y) = 0$, computed using M = 0.5, $k_x = 1$, $k_y = 0$, $Z/\rho_0 c = 0.5 + 0.1i$. The solid and dashed lines denote, respectively, the real and imaginary parts of the dispersion equation. The unstable root is indicated by a circle.

condition (equation (8))) does support instability waves. The existence of Kelvin-Helmholtz-type instability waves in equation (15) was also shown analytically in ref. 4.

On the other hand, when the truncated impedance condition (equation (10)) is applied to the solution given in equation (12), we get a new dispersion relation equation, denoted by $D_{TIM}(\omega, k_x, k_y)$, as:

$$D_{TIM}(\omega, k_x, k_y) \equiv \gamma Z + \rho_0 c(\omega/c - 2Mk_x) = 0. \tag{16}$$

Using the same values of impedance Z, Mach number M and wave numbers k_x and k_y , as that used for Figure 2(a) and (b) plots the contours of Re $\{D_{TIM}(\omega, k_x, k_y)\} = 0$ and Im $\{D_{TIM}(\omega, k_x, k_y)\} = 0$ for the dispersion equation of the TIMIBC. There are now no unstable roots in the upper half ω plane.

To see that equation (16) will indeed not contain any unstable roots, rewrite the equation as

$$\frac{\gamma}{(\omega/c - 2Mk_x)} = -\frac{\rho_0 c}{Z}.$$
 (17)

For the left hand side of equation (17), it can be shown that it maps the upper half of the complex ω plane to the right half of a complex plane. As illustrated in Figure 3, we have that (detailed in the Appendix A), for Im $\{\omega\} > 0$,

$$\operatorname{Re}\left\{\frac{\gamma}{(\omega/c - 2Mk_x)}\right\} > 0. \tag{18}$$

For the right hand side of equation (17), however, because of the passivity condition for the impedance function $Z(\omega)$, namely, $\operatorname{Re}\{Z(\omega)\} \ge 0$ for $\operatorname{Im}\{\omega\} \ge 0$, we have

$$\operatorname{Re}\left\{-\frac{\rho_0 c}{Z}\right\} \le 0. \tag{19}$$

Therefore, it follows that it is not possible for equation (17) to have a root in the upper half ω plane. That is, the dispersion relation equation (equation (16)) for the TIMIBC will contain no instability waves.

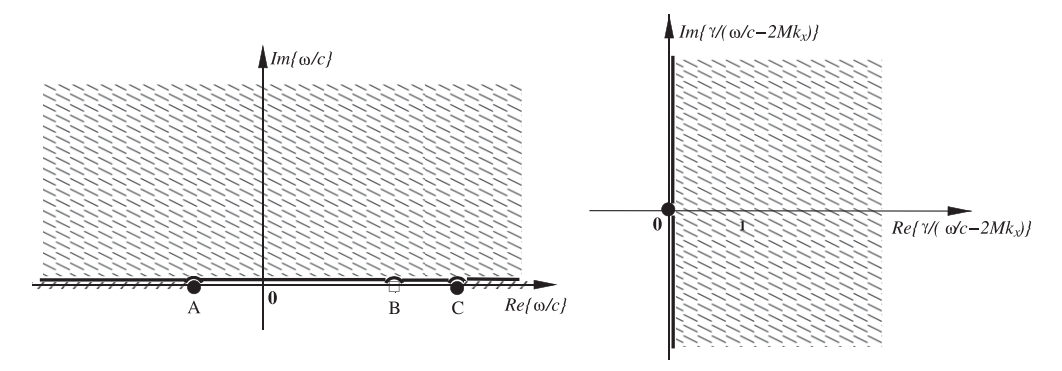


Figure 3. An illustration of mapping by $\gamma/(\omega/c - 2Mk_x)$ of the upper half ω plane. Points A, B, and C have coordinates $(M-1)k_x$, $2Mk_x$, and $(M+1)k_x$ respectively on the real axis. (a) Complex ω/c plane; (b) Mapped $\gamma/(\omega/c - 2Mk_x)$ plane.

Accuracy assessments

The effect of replacing the Ingard-Myers condition (equation (8)) with the TIMIBC (equation (10)) on acoustic reflection by lined surfaces will be assessed using analytical and numerical solutions. Two analytical solutions are discussed in this section, one with plane wave incidence on a lined surface and the other with point source incidence.

Reflection of an incident plane wave

As illustrated in Figure 4, let a two-dimensional incident plane wave onto a lined surface located at z = 0 be denoted as

$$\widehat{p}_{inc} = A_{inc} e^{ik_x x + ik_z z - i\omega t}, \tag{20}$$

where for acoustic waves, we have 18

$$k_x = \left(\frac{\omega}{c}\right) \frac{\cos \theta}{1 + M\cos \theta}, k_z = \left(\frac{\omega}{c}\right) \frac{\sin \theta}{1 + M\cos \theta}.$$
 (21)

Here, M is the mean flow Mach number and θ is the angle between the plane wave vector (k_x, k_z) and the x axis on the x-z plane. Note that, in the current notation, θ is between $-\pi$ and 0 for incident waves as shown in Figure 4.

Let the reflected wave be denoted as

$$\widehat{p}_{ref} = RA_{inc}e^{ik_x x - ik_z z - i\omega t}, \tag{22}$$

where R stands for the reflection coefficient. Then the total pressure field is

$$\widehat{p} = A_{inc} \left(e^{ik_x x + ik_z z - i\omega t} + Re^{ik_x x - ik_z z - i\omega t} \right). \tag{23}$$

When the Ingard-Myers impedance condition (equation (8)) is applied at z = 0, we get

$$-\rho_0(\omega - Uk_x)^2(1+R) = \omega k_z Z(1-R),$$

which gives the reflection coefficient as

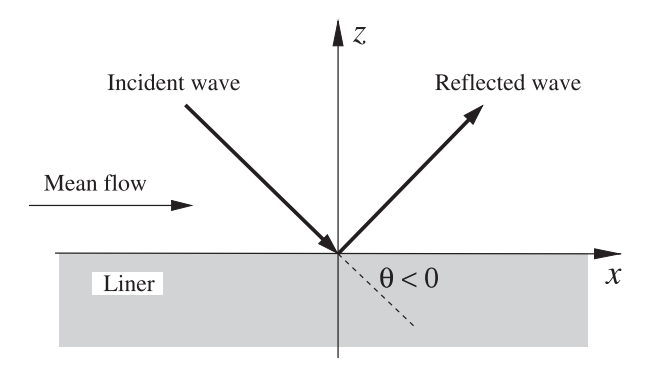


Figure 4. Plane wave reflection by a lined surface at z = 0.

$$R = \frac{\omega k_z Z + \rho_0 (\omega - U k_x)^2}{\omega k_z Z - \rho_0 (\omega - U k_x)^2}.$$
(24)

Using equation (21), it is straightforward to find that, when expressed in incidence angle θ , the reflection coefficient R is

$$R = \frac{Z(1 + M\cos\theta)\sin\theta + \rho_0 c}{Z(1 + M\cos\theta)\sin\theta - \rho_0 c}.$$
 (25)

This expression is identical to the one in Ingard's 1959 paper.¹

On the other hand, applying the truncated Ingard-Myers condition (equation (10)) to the pressure field (equation (23)), and denoting the reflection coefficient as R', we get

$$-\rho_0(\omega - 2Uk_x)(1 + R') = k_z Z(1 - R').$$

This yields the plane wave reflection coefficient as

$$R' = \frac{k_z Z + \rho_0(\omega - 2Uk_x)}{k_z Z - \rho_0(\omega - 2Uk_x)}.$$
 (26)

Expressed in incidence angle θ , again using equation (21), we get

$$R' = \frac{Z(1 + M\cos\theta)\sin\theta + \rho_0 c(1 - M^2\cos^2\theta)}{Z(1 + M\cos\theta)\sin\theta - \rho_0 c(1 - M^2\cos^2\theta)}.$$
 (27)

These two expressions, equations (25) and (27), can now be used to assess the differences in the reflection coefficients between the Ingard-Myers condition and the TIMIBC. Equation (27) clearly shows that the difference in the reflection coefficients between the two conditions will be of order $M^2 \cos^2 \theta$. As such, the differences are generally expected to be small for low Mach number flows where M is small. Furthermore, the two conditions are identical for incident angles of $\theta = 0$, $-\pi/2$, and $-\pi$.

Figure 5 plots the two reflection coefficients, R and R', as functions of the angle of incidence θ , for cases of mean flow Mach number M = 0.3 and 0.6. The impedance value for this example is $Z/\rho_0 c = 0.5 + 0.1i$. It is seen that for the case of Mach number M = 0.3, the reflection coefficients due to the two conditions are very similar for all incident angles. At a higher Mach number M = 0.6, the deviations become larger as expected. We note that different choices of the impedance value Z lead to comparable magnitudes for the difference between R and R'.

To further show the effect of Mach number M, let E denote the difference between R and R' averaged over all incident angles:

$$E = \frac{1}{\pi} \int_{-\pi}^{0} |R - R'| d\theta, \tag{28}$$

and let E_{max} denote the maximum of E over all values of impedance Z within a specified range:

$$E_{\max} = \max_{Z} \{ E | 0 \le \text{Re}\{Z/\rho_0 c\} \le L_R; -L_I \le \text{Im}\{Z/\rho_0 c\} \le L_I \}$$
 (29)

In the current study, the limits for range of the nondimensional resistance and reactance values as defined in equation (29) are set to be $L_R = L_I = 10$. Figure 6 plots the value of E_{max} as a function of the

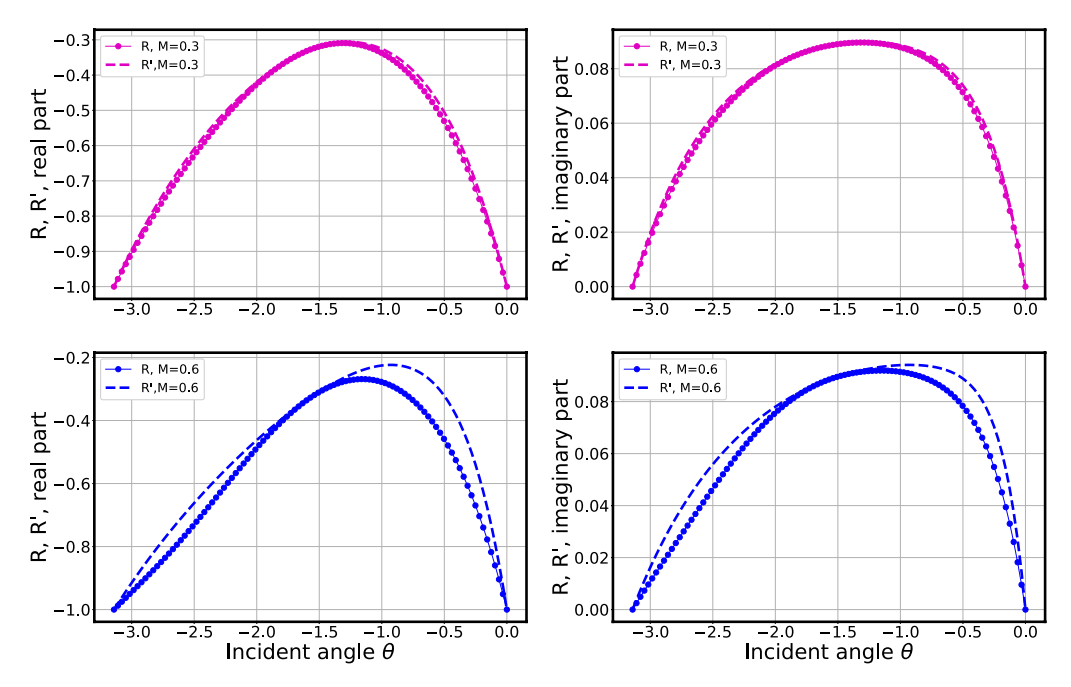


Figure 5. Comparison of reflection coefficients, R by the Ingard-Myers condition, equation (25), and R' by the TIMIBC, equation (27), θ is the plane wave incident angle as defined in Figure 4. The Mach number used in each case is as indicated. $Z/\rho_0c = 0.5 + 0.1i$.

mean flow Mach number M. As expected, the difference increases with M^2 , particularly for small M. It is seen that the difference follows an M^2 trend line closely until the mean flow Mach number is around 0.6.

We note that for a general three-dimensional incident wave of a wave number vector written as

$$k_x = \left(\frac{\omega}{c}\right) \frac{\cos\theta\sin\phi}{1 + M\cos\theta\sin\phi}, k_y = \left(\frac{\omega}{c}\right) \frac{\cos\phi}{1 + M\cos\theta\sin\phi}, k_z = \left(\frac{\omega}{c}\right) \frac{\sin\theta\sin\phi}{1 + M\cos\theta\sin\phi}, \quad (30)$$

in which ϕ denotes the angle between the wave vector (k_x, k_y, k_z) and the y axis, $0 \le \phi \le \pi$, the reflection coefficient is found to be

$$R_{3d} = \frac{Z(1 + M\cos\theta\sin\phi)\sin\theta\sin\phi + \rho_0c}{Z(1 + M\cos\theta\sin\phi)\sin\theta\sin\phi - \rho_0c}$$
(31)

for the Ingard-Myers condition (equation (8)) and

$$R'_{3d} = \frac{Z(1 + M\cos\theta\sin\phi)\sin\theta\sin\phi + \rho_0c(1 - M^2\cos^2\theta\sin^2\phi)}{Z(1 + M\cos\theta\sin\phi)\sin\theta\sin\phi - \rho_0c(1 - M^2\cos^2\theta\sin^2\phi)}$$
(32)

for the TIMIBC (equation (10)). It is seen that the expressions for R_{3d} and R'_{3d} are equivalent to that for R and R', given in equations (25) and (27) respectively, when M is replaced with $M \sin \phi$ and Z is replaced with $Z \sin \phi$. Therefore, the largest difference between the two reflection coefficients would

occur for $\phi = \pi/2$ which results in a two-dimensional plane incidence wave as expressed in equation (21) and analyzed using equations (25) and (27).

Reflection of a point source by a lined surface with flow

In the second example, we consider the reflection of a point source by a lined surface under the Ingard-Myers condition and the TIMIBC condition. Let the point source be located at $\mathbf{r}_0 = (x_0, y_0, z_0), z_0 > 0$, and a planar lined surface of impedance Z be located at z = 0, as illustrated in Figure 7. We assume that the incident acoustic pressure field is the one that satisfies the following convective wave equation with a source term:

$$\left(\frac{\partial}{\partial t} + U \frac{\partial}{\partial x}\right)^2 p - c^2 \nabla^2 p = \delta(\mathbf{r} - \mathbf{r}_0) \delta(t). \tag{33}$$

The frequency domain solution to equation (33) in a free space without any boundary is well-known¹⁸:

$$\widehat{p}_{inc}(\mathbf{r},\omega) = e^{-iM\omega(x-x_0)/a^2c} \frac{e^{i\omega\overline{R}/ac}}{4\pi\alpha c^2\overline{R}},$$
(34)

where again a time dependency of $e^{-i\omega t}$ is assumed, and

$$\overline{R} = \sqrt{(x - x_0)^2 / \alpha^2 + (y - y_0)^2 + (z - z_0)^2}, \alpha = \sqrt{1 - M^2}.$$
 (35)

It is straightforward to show that, similar to the Weyl identity for the regular wave equation of no flow, the incident point source, equation (34), can be expressed in plane waves as follows:

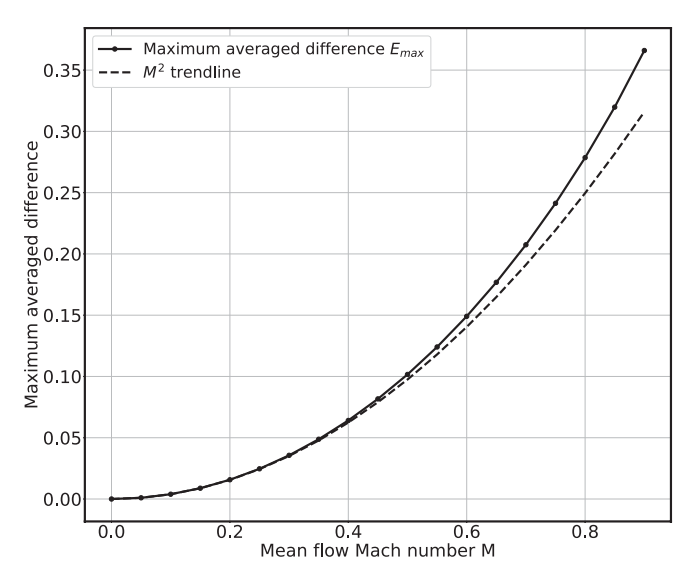


Figure 6. Maximum averaged difference E_{max} , equation (29), as a function of Mach number M.

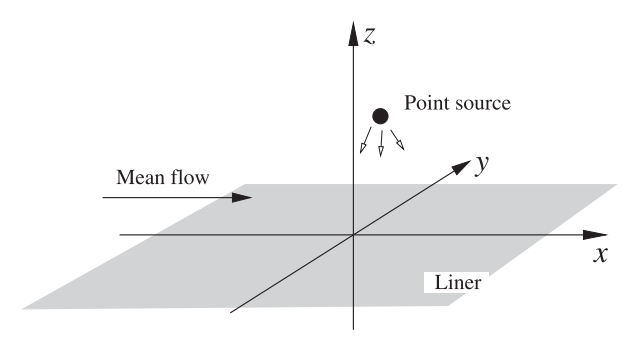


Figure 7. Schematics of a three-dimensional point source incident on a lined surface at z = 0.

$$\widehat{p}_{inc}(\mathbf{r},\omega) = \frac{i}{8\pi^2 c^2} \int_{-\infty}^{\infty} \int_{-\infty}^{\infty} \frac{1}{\gamma} e^{ik_x(x-x_0) + ik_y(y-y_0) + i\gamma|z-z_0|} dk_x dk_y,$$
(36)

where γ is the same as that defined in equations (13) and (14). Let the reflected wave be expressed as

$$\widehat{p}_{ref}(\mathbf{r},\omega) = \frac{i}{8\pi^2 c^2} \int_{-\infty}^{\infty} \int_{-\infty}^{\infty} \frac{R}{\gamma} e^{ik_x(x-x_0) + ik_y(y-y_0) + i\gamma(z+z_0)} dk_x dk_y.$$
(37)

Then, when the Ingard-Myers condition (equation (8)) is applied, we can find that the reflection coefficient R in equation (37) is

$$R = \frac{\omega \gamma Z - \rho_0 (\omega - U k_x)^2}{\omega \gamma Z + \rho_0 (\omega - U k_x)^2},$$
(38)

giving

$$\widehat{p}_{ref}(\mathbf{r},\omega) = \frac{i}{8\pi^2 c^2} \int_{-\infty}^{\infty} \int_{-\infty}^{\infty} \frac{\omega \gamma Z - \rho_0 (\omega - U k_x)^2}{\gamma (\omega \gamma Z + \rho_0 (\omega - U k_x)^2)} e^{ik_x (x - x_0) + ik_y (y - y_0) + i\gamma (z + z_0)} dk_x dk_y.$$
(39)

On the other hand, when the truncated Ingard-Myers condition (equation (10)) is used, the reflection coefficient is found to be the following

$$R' = \frac{\gamma Z - \rho_0(\omega - 2Uk_x)}{\gamma Z + \rho_0(\omega - 2Uk_x)},\tag{40}$$

and the reflected wave is

$$\widehat{p}_{ref}(\mathbf{r},\omega) = \frac{i}{8\pi^2 c^2} \int_{-\infty}^{\infty} \int_{-\infty}^{\infty} \frac{\gamma Z - \rho_0(\omega - 2Uk_x)}{\gamma(\gamma Z + \rho_0(\omega - 2Uk_x))} e^{ik_x(x - x_0) + ik_y(y - y_0) + i\gamma(z + z_0)} dk_x dk_y. \tag{41}$$

Details on numerical evaluation of the integrals in equations (39) and (41) are further discussed in Appendix B.

We now compare the two solutions according to equations (39) and (41). For this example, as illustrated in Figure 8, the point source is located at coordinates (x, y, z) = (0, 0, 1) and impedance of the surface is taken to be $Z/\rho_0c = 0.5 + 0.5i$. The nondimensional frequency is $\omega L/c = 4\pi$ where L stands for a length scale. In Figure 9, solutions for the reflected wave along a field line of $-2 \le x \le 2$,

y = 0, z = 0.5, are plotted. The solutions by the Ingard-Myers condition given in equation (39) are plotted in solid lines and that by the TIMIBC given in equation (41) are plotted in dashed lines. For the case of Mach number M = 0.3, the two solutions are nearly the same. For the case of M = 0.6, the deviations are larger but still appear to be at an acceptable level. Similar magnitudes for the deviations are also found with other choices of the impedance value and wave frequency.

The two examples presented in this section indicate that the proposed TIMIBC would provide a good approximation to the original Ingard-Myers impedance condition for a mean flow of low to mid subsonic Mach numbers.

Time domain implementation of Truncated Ingard-Myers Impedance Boundary Condition

In this section, we present the TIMIBC in the time domain. Specifically, we will provide the time domain TIMIBC in terms of pressure and its normal derivative, as well as in terms of pressure and the normal acoustic velocity.

Multipole expansion approximation of impedance function

We first describe a simple technique of finding the multipole expansion for the acoustic impedance function. Given a set of N_f measurements $Z_j = Z(\omega_j)$, $j = 1, 2, ..., N_f$, suppose the impedance as a function of ω is to be modeled as a rational function $j = 1, 2, ..., N_f$.

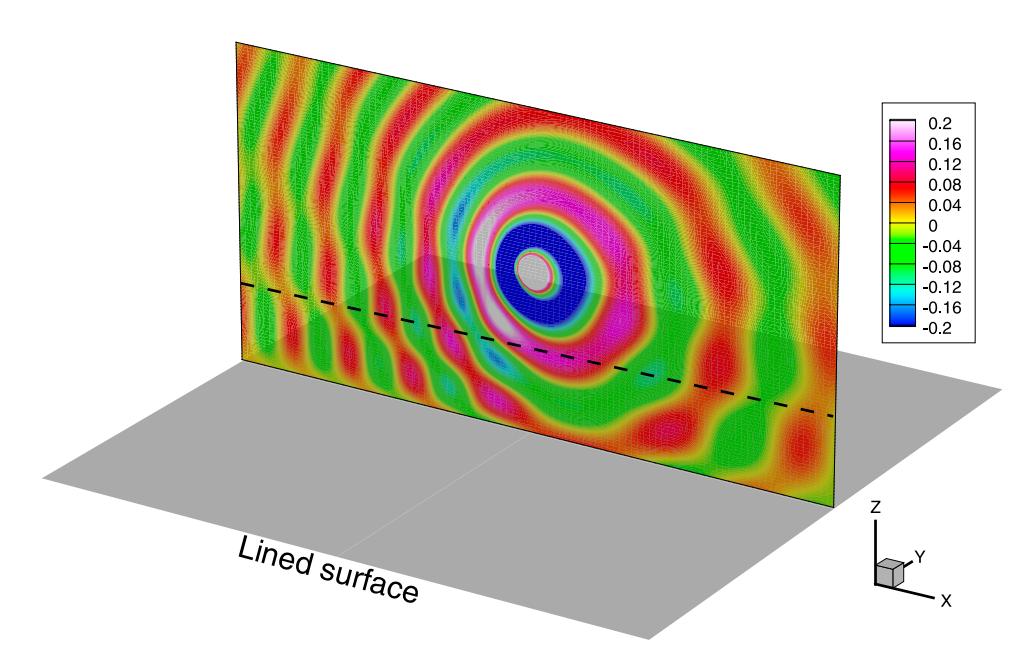


Figure 8. Illustration of a point source reflected by a lined surface. Plotted are the contours of the total pressure field, $\hat{p}_{inc} + \hat{p}_{ref}$, where the point source is located at (0, 0, 1) for a frequency $\omega L/c = 4\pi$, and M = 0.3.

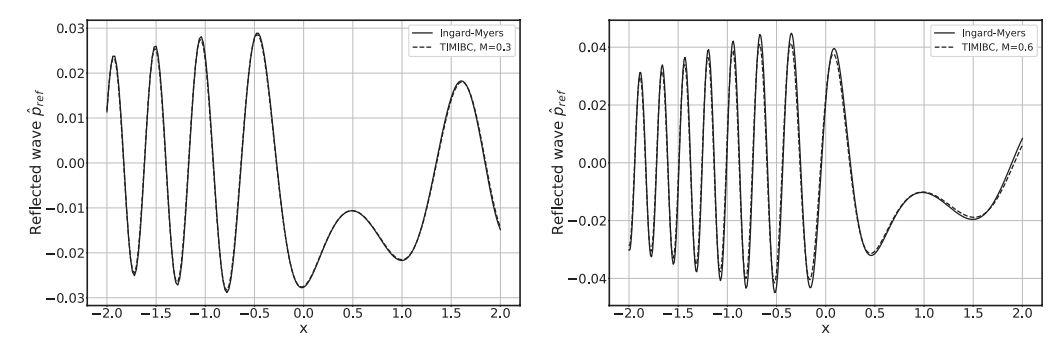


Figure 9. Reflected wave of an incident point source, where the point source is located at (0, 0, 1) with frequency $\omega L/c = 4\pi$. The profiles of reflected waves along a field line of $-2 \le x \le 2$, y = 0, z = 0.5, as indicated by the dotted line in Figure 8, are plotted for the cases of mean flow Mach number (a) M = 0.3 and (b) M = 0.6. The results by the Ingard-Myers condition, equation (39), are plotted in solid lines and that by the TIMIBC, equation (41), are in dashed lines.

$$Z(\omega) = \frac{a_0 + a_1\omega + \dots + a_v\omega^v}{b_0 + b_1\omega + \dots + b_u\omega^u},\tag{42}$$

which, assuming $v \le \mu + 1$, may be equivalently expressed as partial fractions as the following multipole expansion:

$$Z(\omega) = -i\omega h_0 + R_0 + \sum_{m=1}^{N} \frac{A_m}{\lambda_m - i\omega} + \frac{1}{2} \sum_{\uparrow=1}^{L} \left[\frac{B_{\uparrow} + iC_{\uparrow}}{\alpha_{\uparrow} + i\beta_{\uparrow} - i\omega} + \frac{B_{\uparrow} - iC_{\uparrow}}{\alpha_{\uparrow} - i\beta_{\uparrow} - i\omega} \right]. \tag{43}$$

This will be referred to as the broadband multipole expansion model. It contains N+2L poles in the complex ω -plane. In (43), all parameters h_0 , R_0 , λ_m , A_m , a_ℓ , β_ℓ , B_ℓ , C_ℓ assume real values. The values of these parameters are to be determined such that $Z(\omega)$ matches Z_j at $\omega = \omega_j$ as closely as possible. For such a model to be physical, function $Z(\omega)$ should satisfy the conditions for causality, realty, and passivity, $^{4,19,20}_{}$ or be a *positive-real* function as defined in ref. 21:

- 1. (Causality) $Z(\omega)$ is analytic (no poles) in open upper half-plane $Im\{\omega\} > 0$;
- 2. (Realty) $\overline{Z}(\omega) = Z(-\omega)$ for real ω (an overbar denotes complex conjugate);
- 3. (Passivity) Re $\{Z(\omega)\} \ge 0$ for Im $\{\omega\} \ge 0$.

These conditions lead immediately to the requirements that ^{21,22}:

$$h_0, R_0, \lambda_m, \alpha_1 \ge 0$$
and $v \le \mu + 1$. (44)

Currently, a common practice for finding the coefficients and the poles of the multipole model (43) has been to use the vector-fitting method.¹⁵ The vector-fitting method converts a nonlinear optimization problem to a series of linear least square problems. However, a drawback of the vector-fitting method is that the passivity condition is not ensured and needs to be separately checked or enforced.¹⁶ In what follows, we describe a minimization method for finding the poles and coefficients of the multipole model in which the passivity is always satisfied.

We note that for the partial fraction terms in equation (43) we have:

$$\frac{A_m}{\lambda_m - i\omega} = \frac{A_m \lambda_m + i A_m \omega}{\lambda_m^2 + \omega^2},\tag{45}$$

$$\frac{1}{2} \left[\frac{B_{\ell} + iC_{\ell}}{\alpha_{\ell} + i\beta_{\ell} - i\omega} + \frac{B_{\ell} - iC_{\ell}}{\alpha_{\ell} - i\beta_{\ell} - i\omega} \right] \\
= \frac{\left[(\alpha_{\ell}B_{\ell} + \beta_{\ell}C_{\ell}) \left(\alpha_{\ell}^{2} + \beta_{\uparrow}^{2} \right) + \left(\alpha_{\ell}B_{\ell} - \beta_{\ell}C_{\ell} \right) \omega^{2} \right] + i \left[\left(2\alpha_{\ell}\beta_{\ell}C_{\ell} + \left(\alpha_{\ell}^{2} - \beta_{\ell}^{2} \right) B_{\ell} \right) \omega + B_{\ell}\omega^{3} \right]}{\left(\alpha_{\ell}^{2} + \left(\beta_{\ell} - \omega \right)^{2} \right) \left(\alpha_{\ell}^{2} + \left(\beta_{\ell} + \omega \right)^{2} \right)}.$$
(46)

Therefore, passivity of *each* partial fraction term in (43) (those in brackets in case of paired poles), hence $Z(\omega)$ itself, will be ensured if we require further that

$$A_m > 0, \alpha_\ell B_\ell + \beta_\ell C_\ell > 0, \alpha_\ell B_\ell - \beta_\ell C_\ell > 0, \tag{47}$$

in addition to the requirements stipulated in equation (44).

Based on this observation, we propose the following minimization problem for finding the parameters of the multipole model (43):

For a given choice of N and L, find h_0 , R_0 , λ_m , A_m , (m = 1, ..., N), α_ℓ , β_ℓ , γ_ℓ , δ_ℓ , $(\ell = 1, ..., L)$ such that

$$\sum_{j=1}^{N_f} \left| Z(\omega_j; h_0, R_0, \lambda_k, A_k, \alpha_\ell, \beta_\ell, B_\ell, C_\ell) - Z_j \right|^2 = \text{MINIMUM}$$
(48)

subject to

$$(i)h_0, R_0, \lambda_m, \alpha_\ell \ge 0; (ii)A_m, \gamma_\ell, \delta_\ell \ge 0$$

$$(49)$$

where γ_{ℓ} and δ_{ℓ} are related to B_{ℓ} and C_{ℓ} as

$$B_{\ell} = \frac{\gamma_{\ell} + \delta_{\ell}}{2\alpha_{\ell}}, C_{\ell} = \frac{\gamma_{\ell} - \delta_{\ell}}{2\beta_{\ell}}$$

$$\tag{50}$$

The minimization problem (Eq. (48)) is in fact straightforward to program using nonlinear optimization routines. A sample Python script is provided in Appendix C using a differential evolution global optimization algorithm. In general, the values for N and L can start respectively with 1 and 2 and increase as needed.

Time domain impedance boundary condition for the normal pressure derivative

Applying equation (43) to the truncated Ingard-Myers condition (equation (10)), it is straightforward to find the following time domain TIMIBC established for p and $\partial p/\partial n$:

$$h_0 \frac{\partial p_n}{\partial t} + R_0 p_n = -\rho_0 \left(\frac{\partial p}{\partial t} + 2U \frac{\partial p}{\partial x} \right) - \sum_{m=1}^N A_m p_m^{(0)} - \sum_{\ell=1}^L \left[B_\ell p_\ell^{(1)} + C_\ell p_\ell^{(2)} \right], \tag{51}$$

$$\frac{dp_m^{(0)}}{dt} + \lambda_m p_m^{(0)} = p_n, m = 1, ..., N,$$
(52)

$$\frac{dp_{\ell}^{(1)}}{dt} + \alpha_{\ell}p_{\ell}^{(1)} + \beta_{\ell}p_{\ell}^{(2)} = p_{n}, \frac{dp_{\ell}^{(2)}}{dt} + \alpha_{\ell}p_{\ell}^{(2)} - \beta_{\ell}p_{\ell}^{(1)} = 0, \ell = 1, ..., L,$$
(53)

where p_n stands for the normal pressure derivative term $\partial p/\partial n$, and $p_m^{(0)}$, $m=1,\ldots,N$, and $p_{\uparrow}^{(1)}$, $p_{\uparrow}^{(2)}$, $\ell=1,\ldots,L$, are auxiliary variables that are introduced for the convenience of implementation.

Time domain impedance boundary for normal acoustic velocity

The TIMIBC written in pressure p and normal velocity u_n at the boundary has been given in equation (11). Converting into the time domain, we get the following boundary condition written in a system of first-order differential equations for computing u_n at lined boundary points:

$$h_0 \frac{\partial u_n}{\partial t} + R_0 u_n = p + U \frac{\partial g}{\partial x} - \sum_{m=1}^{N} A_m p_m^{(0)} - \sum_{\ell=1}^{L} \left[B_{\ell} p_{\ell}^{(1)} + C_{\ell} p_{\ell}^{(2)} \right], \tag{54}$$

$$\frac{dp_m^{(0)}}{dt} + \lambda_m p_m^{(0)} = u_n, m = 1, ..., N,$$
(55)

$$\frac{dp_{\ell}^{(1)}}{dt} + \alpha_{\ell}p_{\ell}^{(1)} + \beta_{\ell}p_{\ell}^{(2)} = u_{n}, \frac{dp_{\ell}^{(2)}}{dt} + \alpha_{\ell}p_{\ell}^{(2)} - \beta_{\ell}p_{\ell}^{(1)} = 0, \ell = 1, ..., L,$$
 (56)

$$\frac{\partial g}{\partial t} + U \frac{\partial g}{\partial x} = p, \tag{57}$$

where g and $p_m^{(0)}$, m=1,...,N, and $p_\ell^{(1)}$, $p_\uparrow^{(2)}$, $\ell=1,...,L$, are auxiliary variables.

A numerical example

In this section, we show an application of the proposed TIMIBC to a duct acoustics problem. The numerical results will be compared with the NASA Langley Grazing Flow Impedance Tube (GFIT) experimental dataset, ²³ which is commonly used as a benchmark for testing the accuracy of an impedance boundary condition implementation. A diagram of the computational domain, modeled after the GFIT test rig, is shown in Figure 10. The dimensions for the cross section of the rectangular duct are $L_y \times L_z = 0.0635$ m $\times 0.0508$ m. All length units in this section are in meters. A uniform flow of mean velocity U = (U, 0, 0) is assumed. The computational domain extends from x = -0.1 m to x = 1 m. A liner section is placed on the top side of the duct at y = 0.0635 m, from x = 0.2125 m to x = 0.8125 m, as in the GFIT test rig. Additionally, Perfectly Matched Layer (PML) absorbing zones are added at both ends of the rectangular duct to absorb acoustic waves exiting from the interior computational domain. ²⁴

The governing equations used in this example for acoustic wave propagation are the linearized Euler equations of the following form:

$$\frac{\partial \mathbf{u}}{\partial t} + U \frac{\partial \mathbf{u}}{\partial x} + \frac{1}{\rho_0} \nabla p = 0, \tag{58}$$

$$\frac{\partial p}{\partial t} + U \frac{\partial p}{\partial x} + \gamma_0 p_0 \nabla \cdot \boldsymbol{u} = \phi_{m_0 n_0}(y, z) e^{-\sigma_1 x^2} e^{-\sigma_0 t^2}, \tag{59}$$

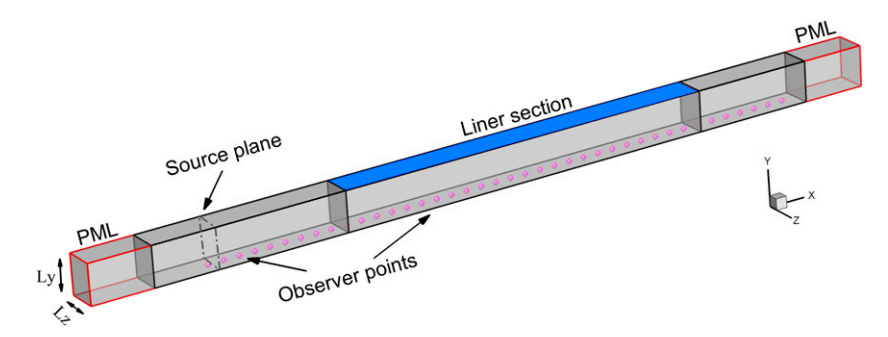


Figure 10. A schematic of computational domain modeled after the GFIT test rig. The liner section is placed at the top side of the duct as indicated. The pressure time history are recorded along the centerline on the side opposite to the liner section shown as the circles. The duct mode is introduced at the location indicated as source plane.

where \boldsymbol{u} and p are respectively the acoustic velocity vector and pressure, ρ_0 and p_0 are respectively the mean density and pressure, and γ_0 is the gas specific heat ratio ($\gamma_0 = 1.4$). The linearized Euler equations (Eqs. (58)–(59)) are solved by a finite difference scheme where the spatial derivatives are discretized by the 7-point DRP scheme ²⁵ and the time integration is carried out by the optimized Runge-Kutta scheme (LDDRK5-6).²⁶ The grid spacings are such that $\Delta x = 0.0025$ m, $\Delta y = 0.00158$ m, $\Delta z = 0.00127$ m, and a nondimensional time step (using speed of the sound and one m as the velocity and length scales) of 0.0004 is used.

The source term appearing in the pressure equation (Eq. 59) is specified in such a way that a duct mode of modal number (m_0, n_0) with a shapefunction/eigenfunction $\phi_{m_0n_0}(y, z)$ can be imposed.²⁷ Here, as in the GFIT experiments, the (0,0) mode is used, i.e., we use $\phi_{00}(y,z) = 1$ for the source term in equation (59). The values for σ_1 and σ_0 in equation (59) are: $\sigma_1 = \ln(2)/(2\Delta x)^2$, $\sigma_0 = \ln(2)/(2\Delta t)^2$. In this way, a broadband time domain plane wave packet is generated at the source plane, which is located at x = 0, as indicated in Figure 10. As the plane wave propagates toward the test section and is scattered by the installed liner section, the effect of the liner impedance condition is simulated. Since the source term is broadband in nature, the effect of the liner for all frequencies can be obtained in one single simulation through an FFT of the time domain solution.

The acoustic liner used in this computation consists of a 2.0 in (0.0508 m) honeycomb core terminated by a rigid backplate and covered with a wire-mesh facesheet of resistance $R = 1.3\rho_0c$. The liner impedance values educed from experimental measurement and their approximation by the multipole expansion of form (equation (43)) are shown in Figure 11. Symbols are the educed values and the dashed lines are the fitted multipole expansion approximation with N = 1 and L = 2. The coefficients for the expansion when normalized by $\rho_0 c$ are as follows:

$$h_0 = 0.035007, R_0 = 0.618771, \lambda_1 = 3.324288, A_1 = 20.033248$$

 $\alpha_1 = 8.608088, \beta_1 = 40.649003, B_1 = 5.559919, C_1 = 1.170545$
 $\alpha_2 = 7.468268, \beta_2 = 25.89168, B_2 = 6.468363, C_2 = 1.822884.$

The time domain TIMIBC for the pressure and boundary normal velocity, namely, equations (54)–(57), is applied at all grid points on the liner section. Specifically, on lined surfaces, u_n , as well

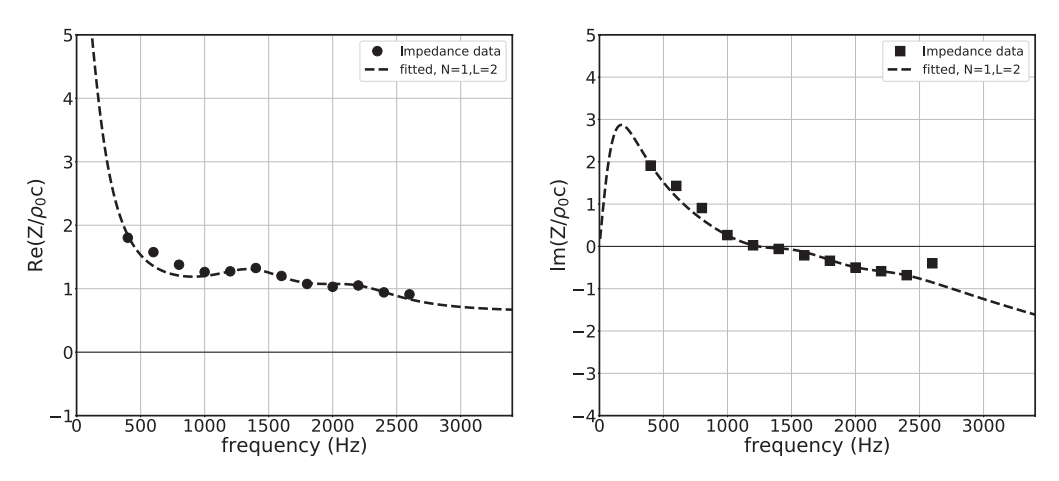


Figure 11. Values of impedance for the liner used in the numerical example. Symbols are the experimentally educed values and the dashed lines are the fitted multipole expansion approximation of the form (43): (a) Resistance, (b) Reactance.

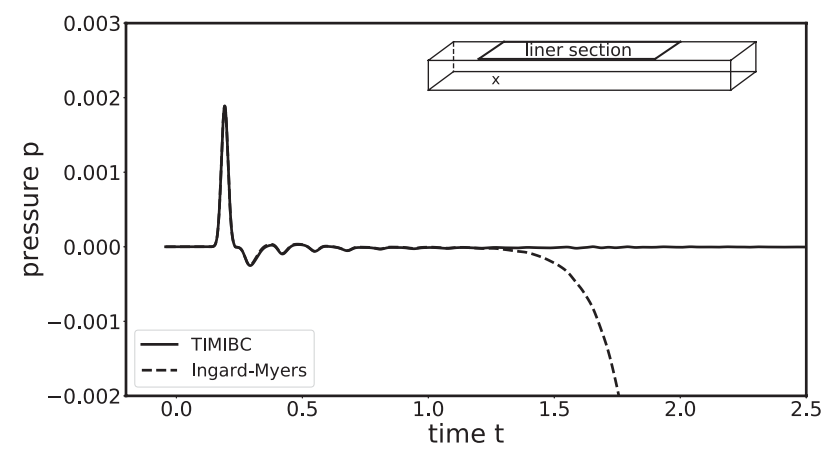


Figure 12. Time history of pressure, nondimensionalized by ρ_0c^2 , at a point (x, y, z) = (0.2 m, 0 m, 0.0254 m), below the leading edge of the liner section as marked by "x" in the insert. The time t is nondimensionalized by using speed of the sound and 1 m as the velocity and length scales. The solutions by the TIMIBC and the Ingard-Myers condition are plotted in solid and dashed lines, respectively. The solution by the Ingard-Myers condition eventually grows exponentially while the solution by the TIMIBC remained stable.

as the auxiliary variables, are found by solving equations (54)–(57) using the same Runge-Kutta time integration scheme as that used for the interior grid points. On solid surfaces, we have $u_n = 0$. To capture the effect of sound attenuation by the liner, the pressure variation along the side of the duct opposite to the liner section is recorded in the computation. Figure 12 shows an example of pressure time history at a sample point on the wall opposite to the liner section with coordinates (x, y, z) = (0.2 m, 0 m, 0.0254 m). Plotted with a solid line is the computational result by the TIMIBC and the result by the original Ingard-Myers impedance condition is plotted as the dashed line. Notice that the solutions by the two conditions are nearly identical initially. However, the numerical solution by the

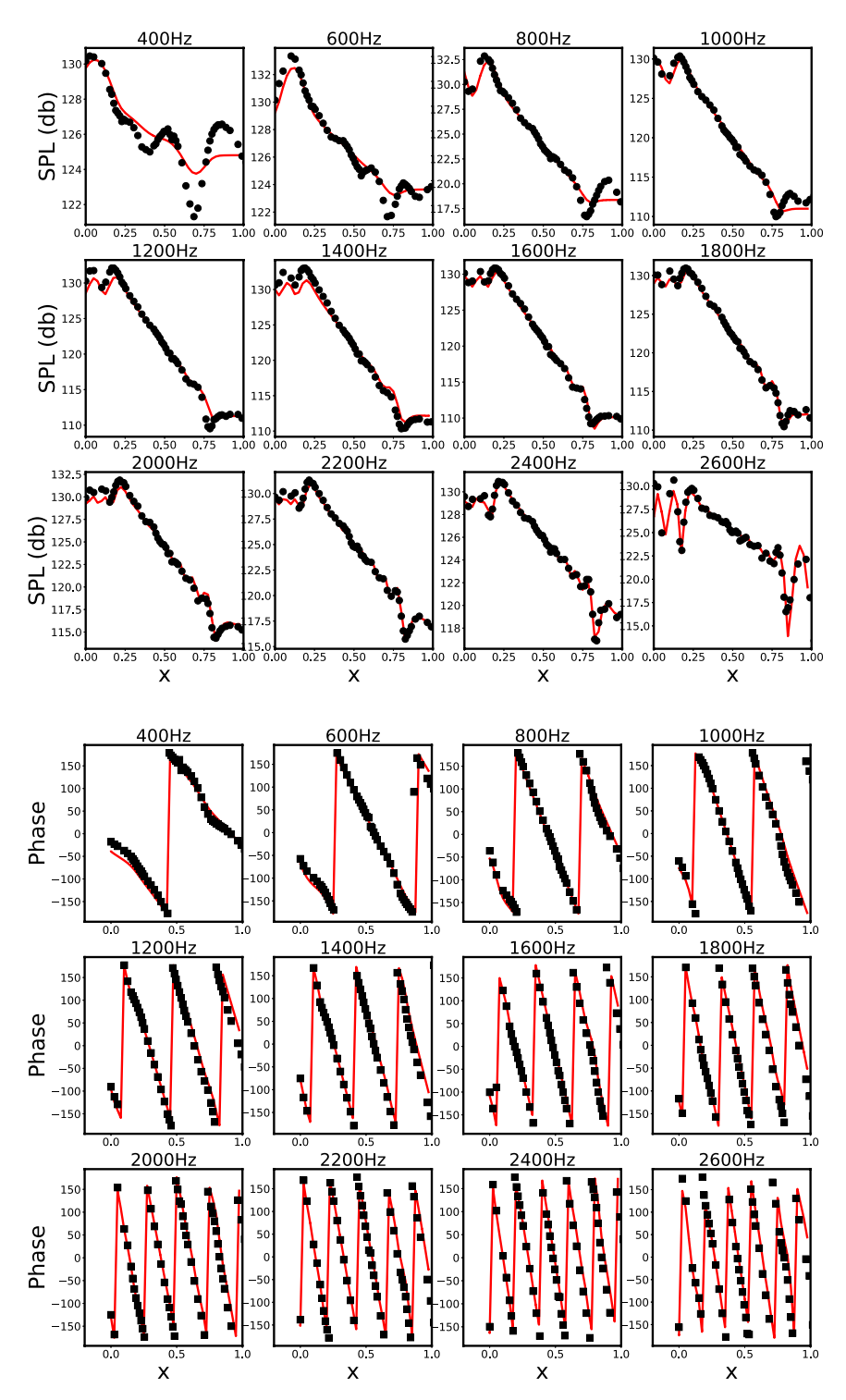


Figure 13. Comparisons of (a) SPL and (b) phase variation along the side of the duct opposite to the liner section. Symbols are the measurements²³ and solid lines are the computational results using the TIMIBC.

original Ingard-Myers condition eventually became unstable while the solution by the TIMIBC remained stable.

Sound attenuation along the side opposite to the liner section is shown in Figure 13 for a range of frequencies from 400 Hz to 2600 Hz. The symbols are the experimental measurements and solid lines are the computed results using the TIMIBC after the time domain solution has been converted to the frequency domain. Very good agreement is observed for both the SPL (Sound Pressure Level) and phase for all the frequencies except perhaps the lowest at 400 Hz, confirming that the impedance values are simulated correctly using the TIMIBC. It should be noted that this behavior at 400 Hz may be due to the specified impedance value and duct termination condition. As mentioned in Ref. 23, low attenuation in the GFIT generally leads to difficulties in the impedance eduction process. In addition, small reflections from the termination may exist at certain frequencies and the resulting standing wave can have greater impact under the low attenuation conditions for this liner at 400 Hz. The effectively anechoic termination provided by the PML condition may exacerbate this situation in the predicted results. Therefore, it is likely that differences between the specified and actual liner impedance, as well as the duct termination conditions, lead to the discrepancy at this frequency.

Conclusions

A stabilization of the Ingard-Myers impedance boundary condition has been proposed. It is formulated by truncating a second-order spatial derivative term when the original Ingard-Myers condition is cast in terms of the acoustic pressure and its surface normal derivative. It is shown analytically that the new formulation is hydrodynamically stable and successfully removes the instability wave that is intrinsic to the original Ingard-Myers formulation. The accuracy of replacing the Ingard-Myers condition with the proposed TIMIBC has been assessed using analytical and numerical solutions. It is found that the TIMIBC can be a good approximation to the Ingard-Myers impedance condition for flows at low to mid subsonic Mach numbers. Furthermore, time domain implementation of the TIMIBC has been formulated. In particular, a minimization procedure for finding the poles and coefficients of the broadband multipole expansion for the impedance function is described in which passivity is ensured. As the Ingard-Myers impedance condition has been shown to be the correct limit as the boundary layer thickness goes to zero, the proposed TIMIBC can offer a practical solution for avoiding the intrinsic instability associated with the original Ingard-Myers formulation in time domain numerical simulations.

Acknowledgements

This work used the computational resources at the Old Dominion University ITS Turing cluster. We also thank the reviewers for helpful comments and suggestions.

Declaration of conflicting interests

The author(s) declared no potential conflicts of interest with respect to the research, authorship, and/or publication of this article.

Funding

The author(s) disclosed receipt of the following financial support for the research, authorship, and/or publication of this article: This research was funded by the Advanced Air Transport Technology (AATT) Project of the NASA Advanced Air Vehicles Program (AAVP) and Aeronautics Research Mission Directorate.

ORCID iDs

Fang Q Hu https://orcid.org/0009-0006-3076-9103 Douglas M Nark https://orcid.org/0000-0001-5548-5904

References

Ingard U. Influence of fluid motion past a plane boundary on sound reflection, absorption, and transmission. J Acoust Soc Am 1959; 31: 1035.

- 2. Myers M. On the acoustic boundary condition in the presence of flow. J Sound Vib 1980; 71: 429-434.
- 3. Tester BJ. The propagation and attenuation of sound in lined ducts containing uniform or "plug" flow. J Sound Vib 1973; 28: 151–203.
- Tam CKW and Auriault L. Time-domain impedance boundary conditions for computational aeroacoustics. AIAA J 1996; 34: 917–923.
- Rienstra SW and Tester BJ. An analytic green's function for a lined circular duct containing uniform mean flow. J Sound Vib 2008; 317: 994–1016.
- Brambley EJ. Fundamental problems with the model of uniform flow over acoustic linings. J Sound Vib 2009; 322: 126–137.
- Brambley EJ and Gabard G. Reflection of an acoustic line source by an impedance surface with uniform flow. J Sound Vib 2014; 333: 5548–5565.
- 8. Rienstra S and Darau M. Boundary-layer thickness effects of the hydrodynamic instability along an impedance wall. *J Fluid Mech* 2011; 671: 559–573.
- Brambley E. Well-posed boundary condition for acoustic liners in straight ducts with flow. AIAA J 2011;
 49: 1272–1282.
- Reymen Y, Baelmans M and Desmet W. Efficient implementation of tam and auriault's time-domain impedance boundary condition. AIAA J 2008; 46: 2368–2376.
- Li XY, Li XD and Tam CKW. Improved multipole broadband and time-domain impedance boundary condition. AIAA J 2012; 50: 980–984.
- Dragna D, Pineau P and Blanc-Benon P. A generalized recursive convolution method for time-domain propagation in porous media. J Acoust Soc Am 2015; 138: 1030–1042.
- Chen C and Li XD. Numerical efficiency analysis of multi-pole time-domain impedance boundary conditions. EUCASS 2019-1034, 2019.
- 14. Hu FQ and Nark DM. On the implementation and further validation of a time domain boundary element method broadband impedance boundary condition. AIAA Paper 2022-2898, 2022.
- Gustavsen B and Semlyen A. Rational approximation of frequency domain responses by vector fitting. IEEE Trans Power Deliv 1999; 14: 1052–1061.
- Gustavsen B and Semlyen A. Enforcing passivity for admittance matrices approximated by rational functions. *IEEE Trans Power Syst* 2001; 16: 97–104.
- Nayfeh AH, Kaiser JE and Telionis DP. Acoustics of aircraft engine-duct systems. AIAA J 1975; 13(2): 130–143.
- 18. Morse PM and Ingard KU. *Theoretical acoustics*. 1st ed. Princeton, NJ: Princeton University Press, 1986.
- 19. Fung KY and Ju H. Time-domain impedance boundary conditions for computational acoustics and aeroacoustics. *Int J Comput Fluid Dyn* 2004; 18: 503.
- Rienstra SW. Impedance models in time-domain including the extended helmholtz resonator model. AIAA paper 2006-2686, 2006.
- 21. Brune O. Synthesis of a finite two-terminal network whose driving-point impedance is a prescribed function of frequency. *J Math Phys* 1931; 10: 191–236.
- 22. Chen WK. Passive, active, and digital filters. Boca Raton, FL: CRC Press, 2009.

- Jones M and Watson W. On the use of experimental methods to improve confidence in educed impedance.
 AIAA Paper 2011-2865, 2011.
- 24. Hu FQ. Absorbing boundary conditions. Int J Comput Fluid Dyn 2004; 18(6): 513-522.
- Tam CKW and Webb JC. Dispersion-relation-preserving finite difference schemes for computational acoustics. J Comput Phys 1993; 107: 262–281.
- Hu FQ, Hussaini MY and Manthey JL. Low-dissipation and low-dispersion Runge-Kutta schemes for computational acoustics. J Comput Phys 1996; 124: 177–191.
- 27. Hu FQ, Kocaogul I and Li XD. On the adjoint problem in duct acoustics and its solution by the time domain wave packet method. AIAA Paper 2012-2247, 2012.
- 28. Hu FQ, Pizzo ME and Nark DM. On a time domain boundary integral equation formulation for acoustic scattering by rigid bodies in uniform mean flow. *J Acoust Soc Am* 2017; 142: 3624–3636.
- 29. Squire HB. On the stability for three-dimensional disturbances of viscous fluid flow between parallel walls. *Proc Roy Soc Lond* 1933; 142: 621–628.
- Zheng S and Zhuang M. Three-dimensional benchmark problem for broadband time-domain impedance boundary conditions. AIAA J 2004; 42: 405–407.

Appendix A

In this appendix, we show that equation (18) is true for any value of ω on the upper half ω plane. That is, we want to show that, for $\text{Im}\{\omega\} > 0$, we have

$$-\frac{\pi}{2} < \arg\left\{ \frac{\sqrt{(\omega/c - Mk_x)^2 - k_x^2 - k_y^2}}{(\omega/c - 2Mk_x)} \right\} < \frac{\pi}{2},\tag{60}$$

where arg {} stands for the argument of the complex expression inside the bracket. First, consider the case when $k_y = 0$. As illustrated in Figure 14, for any ω on the upper half plane, noted by point D, we have

$$\arg\left\{\frac{\sqrt{(\omega/c - Mk_x)^2 - k_x^2}}{(\omega/c - 2Mk_x)}\right\} = \frac{\alpha_1 + \alpha_2}{2} - \beta = \frac{\alpha_2 - \beta}{2} - \frac{\beta - \alpha_1}{2} = \frac{\theta_2}{2} - \frac{\theta_1}{2},\tag{61}$$

for any real value of k_x and a subsonic Mach number M.

Now considering triangles $\triangle ADB$ and $\triangle BDC$, we obviously have

$$0 < \theta_1 < \pi, 0 < \theta_2 < \pi. \tag{62}$$

Then, it follows immediately that

$$-\frac{\pi}{2} < \frac{\theta_2}{2} - \frac{\theta_1}{2} < \frac{\pi}{2}.\tag{63}$$

Hence, equation (60) is true when $k_y = 0$. While Figure 14 assumes $k_x > 0$, it can be shown similarly that equation (60) is true for $k_x < 0$ as well.

If $k_y \neq 0$, the expression inside the bracket of equation (60) can be written equivalently using the Squire transformation²⁹ as

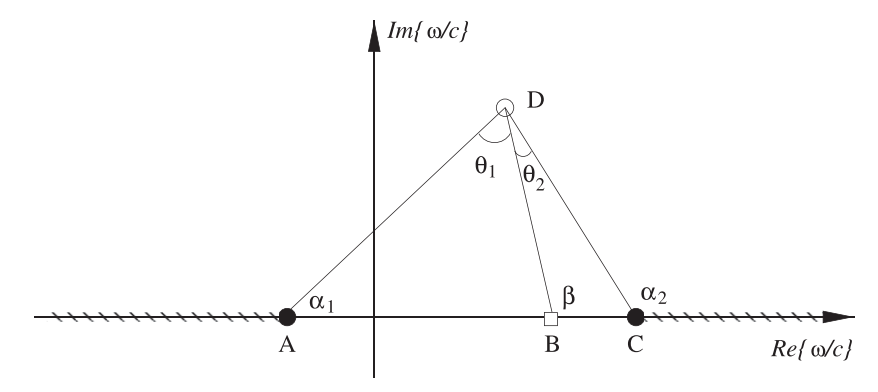


Figure 14. An illustration for the mapping property shown in equation (18). Crossed lines indicate the branch cuts for $\sqrt{(\omega/c-Mk_x)^2-k_x^2}$. Points A, B, and C have coordinates $(M-1)k_x$, $2Mk_x$, and $(M+1)k_x$, respectively, on the real axis. Point D represents an arbitrary point in the upper half ω plane.

$$\frac{\sqrt{\left(\omega/c - Mk_x\right)^2 - k_x^2 - k_y^2}}{\left(\omega/c - 2Mk_x\right)} = \frac{\sqrt{\left(\omega/c - \widehat{M}\widehat{k}_x\right)^2 - \widehat{k}_x^2}}{\left(\omega/c - 2\widehat{M}\widehat{k}_x\right)},\tag{64}$$

where

$$\widehat{k}_x = \sqrt{k_x^2 + k_y^2}, \widehat{M} = \frac{k_x}{\widehat{k}_x} M. \tag{65}$$

This again leads to equation (60) with $k_y = 0$ and k_x , M being replaced respectively by \hat{k}_x , \hat{M} .

Appendix B

To facilitate numerical evaluation of the integrals in equation (39) that have infinite limits, similar to Ref. 30 in the case of no flow, consider a change of variables from (k_x, k_y) to (u, v) as

$$k_x = u\cos v - \frac{M\omega}{\alpha^2 c}, k_y = \alpha u\sin v. \tag{66}$$

Then, we have

$$\gamma = \alpha \sqrt{\left(\frac{\omega}{\alpha^2 c}\right)^2 - u^2},\tag{67}$$

and equation (39) can be written as follows:

$$\widehat{p}_{ref} = \frac{ie^{-i\frac{M\omega}{\alpha^{2}c}(x-x_{0})}}{8\pi^{2}c^{2}} \int_{0}^{2\pi} \int_{0}^{\infty} \frac{\left(\omega\gamma Z - \rho_{0}(\omega/\alpha^{2} - Uu\cos\nu)^{2}\right)}{\gamma\left(\omega\gamma Z + \rho_{0}(\omega/\alpha^{2} - Uu\cos\nu)^{2}\right)} e^{iu(x-x_{0})\cos\nu + iau(y-y_{0})\sin\nu + i\gamma(z+z_{0})} aududv.$$
(68)

Furthermore, by a change of variable from u to ξ such that:

for $0 < u < \frac{\omega}{a^2c}$

$$u = \frac{\omega}{a^2 c} \sqrt{1 - \xi^2}, \gamma = \xi \left(\frac{\omega}{ac}\right),\tag{69}$$

and for $\frac{\omega}{\alpha^2 c} < u < \infty$,

$$u = \frac{\omega}{\alpha^2 c} \sqrt{1 + \xi^2}, \gamma = i\xi \left(\frac{\omega}{\alpha c}\right). \tag{70}$$

The reflected wave (equation (68)) can be further expressed as

$$\begin{split} \widehat{p}_{ref} &= \frac{i\tilde{k}e^{-i\tilde{k}M(\tilde{x}-\tilde{x}_{0})}}{8\pi^{2}c^{2}\alpha} \int_{0}^{2\pi} \int_{0}^{1} \frac{\left(\alpha^{3}\xi\overline{Z} - \left(1 - M\sqrt{1 - \xi^{2}}\cos\nu\right)^{2}\right)}{\left(\alpha^{3}\xi\overline{Z} + \left(1 - M\sqrt{1 - \xi^{2}}\cos\nu\right)^{2}\right)} \\ e^{i\tilde{k}\sqrt{1 - \xi^{2}}((\tilde{x}-\tilde{x}_{0})\cos\nu + (\nu-\nu_{0})\sin\nu) + i\tilde{k}\xi(z+z_{0})} d\xi d\nu \\ &+ \frac{\tilde{k}e^{-i\tilde{k}M(\tilde{x}-\tilde{x}_{0})}}{8\pi^{2}c^{2}\alpha} \int_{0}^{2\pi} \int_{0}^{\infty} \frac{\left(i\alpha^{3}\xi\overline{Z} - \left(1 - M\sqrt{1 + \xi^{2}}\cos\nu\right)^{2}\right)}{\left(i\alpha^{3}\xi\overline{Z} + \left(1 - M\sqrt{1 + \xi^{2}}\cos\nu\right)^{2}\right)} \\ e^{i\tilde{k}\sqrt{1 + \xi^{2}}((\tilde{x}-\tilde{x}_{0})\cos\nu + (\nu-\nu_{0})\sin\nu) - \tilde{k}\xi(z+z_{0})} d\xi d\nu \end{split}$$

where

$$\tilde{k} = \frac{\omega}{\alpha c}, \tilde{x} = \frac{x}{\alpha}, \overline{Z} = \frac{Z}{\rho_0 c}.$$

Note that the integrand for the second ξ integral now decays exponentially as $\xi \to \infty$. Similarly, when expressed again in integrals using ξ and ν , the reflected wave by the TIMIBC as given in equation (41) can be evaluated using the following form:

$$\begin{split} \widehat{p}_{ref} &= \frac{i\tilde{k}e^{-i\tilde{k}M(\tilde{x}-\tilde{x}_0)}}{8\pi^2c^2\alpha} \int_0^{2\pi} \int_0^1 \frac{\left(\alpha\xi\overline{Z} - \left(1 + M^2 - 2M\sqrt{1 - \xi^2}\cos\nu\right)\right)}{\left(\alpha\xi\overline{Z} + \left(1 + M^2 - 2M\sqrt{1 - \xi^2}\cos\nu\right)\right)} \\ &e^{i\tilde{k}\sqrt{1 - \xi^2}((\tilde{x}-\tilde{x}_0)\cos\nu + (\nu-\nu_0)\sin\nu) + i\tilde{k}\xi(z+z_0)} d\xi d\nu \\ &+ \frac{\tilde{k}e^{-i\tilde{k}M(\tilde{x}-\tilde{x}_0)}}{8\pi^2c^2\alpha} \int_0^{2\pi} \int_0^\infty \frac{\left(i\alpha\xi\overline{Z} - \left(1 + M^2 - 2M\sqrt{1 + \xi^2}\cos\nu\right)\right)}{\left(i\alpha\xi\overline{Z} + \left(1 + M^2 - 2M\sqrt{1 + \xi^2}\cos\nu\right)\right)} \\ &e^{i\tilde{k}\sqrt{1 + \xi^2}((\tilde{x}-\tilde{x}_0)\cos\nu + (\nu-\nu_0)\sin\nu) - \tilde{k}\xi(z+z_0)} d\xi d\nu. \end{split}$$

Appendix C

In this Appendix, a sample Python script for finding the coefficients in the multipole expansion (equation (43)) by the optimization procedure described in the present paper is given below. The

required input file and values are: impedance.dat, data file of experimentally educed impedance; N, number of single poles; L, number of paired poles. The format for each row of data in impedance.dat is assumed to be of the following: $f \ \overline{Z}_r \ \overline{Z}_i$.

where f is frequency in Hz, and \overline{Z}_r and \overline{Z}_i are respectively the corresponding resistance and reactance of the liner, nondimensionalized by $\rho_0 c$ and under $e^{-i\omega t}$ time dependency assumption.

```
import numpy as np
     import scipy.optimize as sp opt
     def objective func(x, omega, Z data, N, L):
       h0, R0, A, gamma, B, C, alpha, beta = get <math>coef(x, N, L)
       Z val = Z func(omega, h0, R0, A, gamma, B, C, alpha, beta)
       obj val = np.absolute(Z val-Z data).sum()
       return obj val
     def get coef(x, N, L):
       h0 = x[2*N + 4*L + 1]; R0 = x[2*N + 4*L]; A = []; gamma = []; B = []; C = []; alpha = [];
beta = []
       for i in range(N):
          A.append(x[2*j]); gamma.append(x[2*j+1])
       for j in range(L):
          B.append((x[2*N + 4*i] + x[2*N + 4*i + 1])/(2.0*x[2*N + 4*i + 2]))
          C.append((x[2*N + 4*i]-x[2*N + 4*i + 1])/(2.0*x[2*N + 4*i + 3]))
          alpha.append(x[2*N + 4*j + 2]); beta.append(x[2*N + 4*j + 3])
       return h0, R0, A, gamma, B, C, alpha, beta
     def Z func(omega, h0, R0, A, gamma, B, C, alpha, beta):
       Z = -1i*omega*h0 + R0
       for Ak, lk in zip(A,gamma):
          Z = Z + Ak/(lk-1j*omega)
       for Bk, Ck, alf, bta in zip(B, C, alpha, beta):
          Z = Z + 0.5*(Bk + 1j*Ck)/(alf + 1j*bta-1j*omega)+0.5*(Bk-1j*Ck)/(alf-1j*bta-1j*omega)
1j*omega)
       return Z
     if name__ == '__main__':
       N = 1 #choose number of single poles
       L = 2 #choose number of paired poles
       c = 343.00 #speed of sound to be used, in (m/s)
       Z input = np.loadtxt('impedance.dat')
       omega = Z input[:,0]*2.0*np.pi/c #non-dimensionalization of frequency
       Z data = Z input[:,1]+1j*Z input[:,2] #resistance and reactance (2nd and 3rd column)
     # optimization for impedance fitting
     #=
       fargs = (omega, Z data, N, L); bnds max = 2.0*max(omega);
       fbnds = [(0, bnds max)]*(2*N + 4*L + 2)
       res = sp opt.differential evolution(objective func, bounds = fbnds, args = fargs,
       maxiter = 2000, popsize = 50, tol = 1.e-2,
       callback = None
       h0, R0, A, gamma, B, C, alpha, beta = get coef(res.x, N, L)
```